



Using deep learning to assimilate sun-induced fluorescence satellite observations in the ISBA land surface model

Pierre Vanderbecken¹, Jasmin Vural¹, Oscar Rojas-Muñoz¹, Sebastien Garrigues², Bertrand Bonan¹, Cedric Bacour⁴, Uwe Rasher³, Bastian Siegmann³, Patricia de Rosnay², and Jean-Christophe Calvet¹

¹Météo-France, CNRS, Univ. Toulouse, CNRM, Toulouse, France.

²ECMWF, Reading, UK and Bonn, Germany

³Institute of Bio- and Geosciences, IBG-2: Plant Sciences, Forschungszentrum Jülich GmbH, Leo-Brandt-Str., 52425 Jülich, Germany

⁴Laboratoire des Sciences du Climat et de l'Environnement, LSCE/IPSL, CEA-CNRS-UVSQ, Université Paris-Saclay, Gif-sur-Yvette, France

Correspondence: Jean-Christophe Calvet (jean-christophe.calvet@meteo.fr)

Abstract.

Accurate representations of the surface and vegetation are critical for simulating the terrestrial CO₂ cycle in response to climate and meteorological conditions. To meet this challenge, an increasing number of satellite missions are being launched which can monitor vegetation conditions and biomass. One is the Copernicus Sentinel-5P mission, which carries the TROPOMI instrument and retrieves Solar-Induced Chlorophyll Fluorescence (SIF). As an indicator of plant photosynthetic activity, SIF can provide critical information for evaluating and parameterising gross carbon flux dynamics in surface models. This study aims to assimilate TROPOMI SIF data into the ISBA (Interactions between Soil, Biosphere and Atmosphere) land surface model developed by Météo-France, with the objective of directly correcting the representation of Leaf Area Index (LAI) and Gross Primary Production (GPP). To achieve this, we have developed a dedicated observation operator that links the modelled LAI to the TROPOMI SIF daily product. This neural network operator was developed using deep learning and was trained using observations over Europe. This operator achieved good accuracy, was implemented in a land data assimilation system (LDAS), and was used to assimilate TROPOMI SIF in ISBA using a sequential simplified extended Kalman filter. Specific experiments were conducted to study the assimilation process over the Ebro basin in Spain. This area is known for its irrigated croplands, which are not well represented by ISBA. Some experiments assimilate TROPOMI SIF, some assimilate a Copernicus Land Monitoring Service (CLMS) LAI 10-day product, and some assimilate both. This provided us with a useful point of reference for improving the vegetation simulation. Following SIF assimilation, LAI representation improved across the domain, highlighting heavily irrigated croplands. The gross primary production (GPP) derived from the analysis is closing the gap between the simulated and observed values, though a significant difference remains. When compared with other assimilation experiments, assimilating SIF alone provides a similar benefit to standard assimilation of a CLMS LAI product on LAI and GPP. The best improvements to the LAI and GPP results come from co-assimilating TROPOMI SIF with the CLMS LAI product, which combines the advantages of high-frequency SIF observations and robust 10-day LAI assimilation.



1 Introduction

Monitoring the carbon cycle in near real time at city, regional and national scales helps decision-makers track the effectiveness of environmental policies in the context of climate change mitigation and emission reduction efforts (Horowitz, 2016). One of the main efforts at the European level was to develop and maintain a new operational monitoring and verification support capacity (CO2MVS) for the carbon cycle. It has been demonstrated that the natural carbon flux of the land surface is the most uncertain component of the carbon budget (Agustí-Panareda et al., 2022; Friedlingstein et al., 2025). Near real-time monitoring requires a joint analysis of the water and carbon cycles. Incorporating new observations of soil moisture and vegetation variables, such as Leaf Area Index (LAI), into land surface models can enhance the precision of these systems (Sabater et al., 2008; Albergel et al., 2020). One promising type of observation is the remote sensing of solar-induced chlorophyll fluorescence (SIF) in vegetation (Bolhar-Nordenkamp et al., 1989; Moya et al., 2004). Solar radiation flux is absorbed by chlorophyll, enabling photosynthesis and fuelling biological fluorescence in the near-infrared and far-red regions of the spectrum (Berry, 2018). SIF has distinctive spectral maxima that can be extracted from Top of Atmosphere (TOA) radiance measurements taken in space (Köhler et al., 2015; Joiner et al., 2016). Recently, SIF was retrieved on the large swath of the Copernicus Sentinel-5 Precursor instrument: TROPOMI (Köhler et al., 2018; Guanter et al., 2021). It provides a daily estimate of SIF in the near-infrared spectrum. SIF observations have been shown to correlate strongly with leaf area index (LAI), gross primary production (GPP) and other vegetation monitoring variables (Leroux et al., 2018; Butterfield et al., 2023). It has also been used to optimise the parameterisation of vegetation simulation models by Bacour et al. (2019).

Advances in artificial intelligence have led to its growing use in geoscientific research (Jiang et al., 2020; Sun et al., 2022). Although computationally demanding physical models are usually employed to simulate complex physics, statistical non-linear models can sometimes achieve greater accuracy (Lang et al., 2024). Furthermore, once trained, these statistical models are faster and better suited to the requirements of an operational system. However, this speed gain comes at the cost of reduced understanding of the physical processes involved. Nevertheless, some tools are beginning to emerge to interpret the behaviour of statistical models (Molnar, 2020). Deep learning is based on the supervised training of an artificial neural network using a large database (Schmidhuber, 2015). To enable more real-time and operational monitoring of vegetation, the 8-day TROPOMI SIF retrieval has been assimilated into the IFS land surface model developed at ECMWF at a global scale (Garrigues et al., 2026). In this study, we propose to constrain simulations from the ISBA (Interactions between Soil, Biomass and Atmosphere) land surface model, which is developed at Météo-France and available through the SURFEX (SURFace EXternalisée) platform (Masson et al., 2013; Decharme et al., 2013), by assimilating the daily retrieval of TROPOMI SIF. As the SIF is not explicitly simulated by this model, a new observation operator is required to map the model variables into observation space. A process-based SIF observation operator is complex, requiring significant computational resources to accurately solve the radiative processes and calibration to reduce associated uncertainties. This makes it difficult to implement such an observation operator in an operational system. An alternative machine learning-based operator for SIF seems more suitable. TROPOMI



55 SIF provides daily global retrievals, which will serve as our database for developing and training a neural network observa-
tion operator. Corchia et al. (2023) have successfully achieved the assimilation of new observations in the ISBA land surface
model using a neural network observation operator for ASCAT (ESA Advanced Scatterometer) backscattering observations.
We adapted this methodology and applied it to the assimilation of TROPOMI SIF.

This article describes the design of the regional deep learning observation operator for SIF measurements and its use in
60 a sequential assimilation process to constrain simulations produced by the ISBA land and vegetation surface model within
the SURFEX platform. The benefits of assimilating TROPOMI SIF data will be evaluated in the Ebro basin. This specific
region was chosen because the land surface model does not represent the heavily irrigated croplands resulting from field
management. TROPOMI SIF assimilation can correct this. The next section presents the methods including the dataset, land
data assimilation and the deep learning operator. Section three is dedicated to the results, beginning with an evaluation of the
65 observation operator and the different assimilation strategies for TROPOMI SIF, alongside different observation errors or co-
assimilation with LAI. Section four discusses the results and outlines the limitations and upcoming challenges of systematically
assimilating TROPOMI SIF. The conclusions are drawn in the final section.

2 Method

2.1 Datasets

70 2.1.1 Domain

All the datasets for the training of the observation operator are extracted on a large regional domain. The database domain
covers Europe, extending from 26°W to 46°E and from 28°N to 72°N. The grid is uniform and regular with a resolution of
0.1°. This domain is the same domain as that used by Hamer et al. (2025). Grid cells of vegetation are selected within this
domain using the ECOCLIMAP-II land cover classification (Faroux et al., 2013), which is available in SURFEX. Figure 1
75 illustrates the most common vegetation type found within each grid cell. In ISBA, urban areas are considered as bare rock. As
such, urban areas are also displayed as bare rock in Fig. 1. In terms of low vegetation, Europe is dominated by C3-grassland
and C3-crops, with forests of mixed deciduous and coniferous trees in higher latitudes. The zoom in Fig. 1 is on the Ebro and
Rio Segre basins in Spain. This region is well known for its heavily irrigated crop fields, which are usually difficult to model
accurately.

80 2.1.2 SIF databases

TROPOMI SIF is a high-level product obtained from the atmospheric reflectivity data collected by the Sentinel-5P SWIR
instrument as part of the TROPOSIF project (Guanter et al., 2021). The distributed data ranges from May 2018 to December
2021 for the project, but the same process is now operational on the online data portal that distributes the product. Here,
we used the data from the TROPOSIF project. Sentinel-5P operates on a heliosynchronous orbit and, with a swath of 2,600
85 km, passes over a given region at least once a day (Veefkind et al., 2012). The nadir measurement crosses the equator at

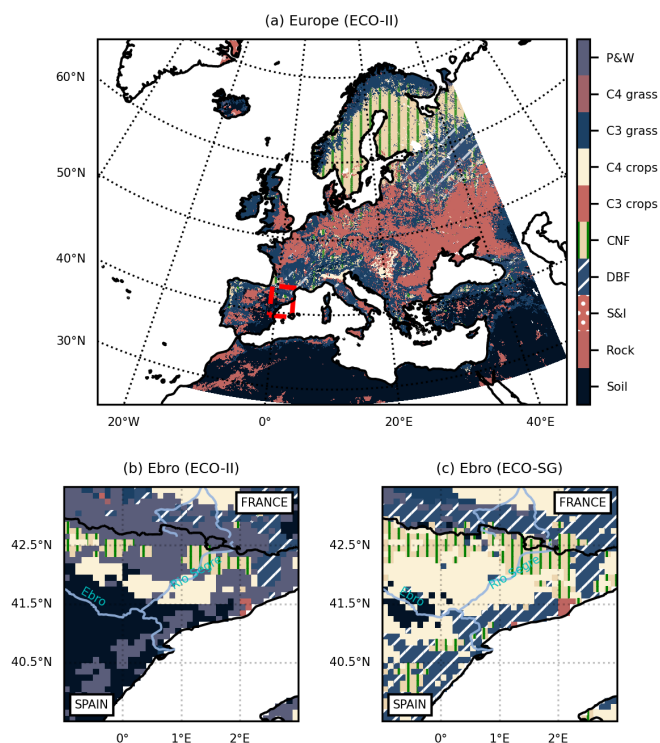


Figure 1. Dominant Plant Functional Type according to land use maps. (a) Domain Europe with ECOCLIMAP-II [26°W to 46°E, 28 to 72°N], the delimited area in red represents the Ebro basin subdomain. (b) The Ebro basin subdomain [1°W to 3°E, 39.5 to 43.5°N] with ECOCLIMAP II. (c) The Ebro basin subdomain with ECOCLIMAP-SG. The 12 PFT are from bottom to top: bare soil, rocks, snow and ice-S&I, deciduous broadleaves forest-DBF, Coniferous needle forest-CNF, C3 croplands, C4 croplands-C4, C3 grassland, C4 grassland, Peat and Wetlands- P&W.

13h30 local solar time, achieving a resolution of 7km×3.5km. The retrieval process involves the statistical modelling of TOA radiances over vegetation, while excluding the signal induced by the underlying bare surface. Surface vegetation is described using the MODIS2018 database (Friedl and Sulla-Menashe, 2015). Using prior knowledge of the solar-induced fluorescence spectrum, the algorithm extracts the SIF-related part of the TOA radiance signal (Guanter et al., 2015). The estimated SIF is then computed by subtracting the expected radiance of the bare soil from the TOA signal. This process ensures that the distribution of TROPOMI SIF observations is centred on zero over bare soil. This means that negative values for TROPOMI SIF can occur, which we have discarded. TROPOMI SIF measurements correspond to the near-infrared peak of the SIF spectrum. Instantaneous estimates are computed according to a spectral window between 743 and 753 nm. The estimates are robust to cloud contamination. Alongside these instantaneous estimates, the Level-2 TROPOMI SIF product provides a corrected value according to day length and solar angle at a given latitude (Köhler et al., 2018). As the model domain is defined on a regular

90

95



grid, the observations must be interpolated. All positive instantaneous measurements from a given day covering a grid cell in the domain are averaged to provide a value for that grid cell.

In July 2021, an airborne SIF measurement campaign was conducted over the irrigated fields of the Ebro basin (Rascher et al., 2015), which lies within the grid cell used for the previous time series. The measurement resolution is approximately 100 10 m and the observed area is primarily covered by C3 crops and bare soil.

2.1.3 LAI and GPP observations

To complete the training and evaluation of vegetation monitoring, we considered two additional types of vegetation observation: LAI (leaf area index) and GPP (gross primary production). The LAI satellite products used here are provided by the Copernicus Land Monitoring Service (CLMS). LAI-V1 is an observation-driven product with a resolution of 1 km, based on measurements 105 from the SPOT-VGT satellite (from 1999 to 2014) and the PROBA-V satellite (from 2014 to June 2020). It provides an estimation of LAI at a global scale every 10 days. To align with our daily TROPOMI SIF product, the LAI maps undergo linear time interpolation. Time interpolation is only performed between observations separated by 10 days; if an observation is missing, the gap is not filled. As in previous studies (Albergel et al., 2010; Barbu et al., 2011; Corchia et al., 2023, among others), LAI observations are interpolated to the spatial resolution of the model grid points using an arithmetic average if at 110 least 50% of the grid points are observed (i.e. half the maximum amount). As the LAI-V1 product is no longer available after June 2020, we will use CLMS LAI raster at a resolution of 300 m instead for later dates instead. This provides data every 10 days and is spatially interpolated in the same way.

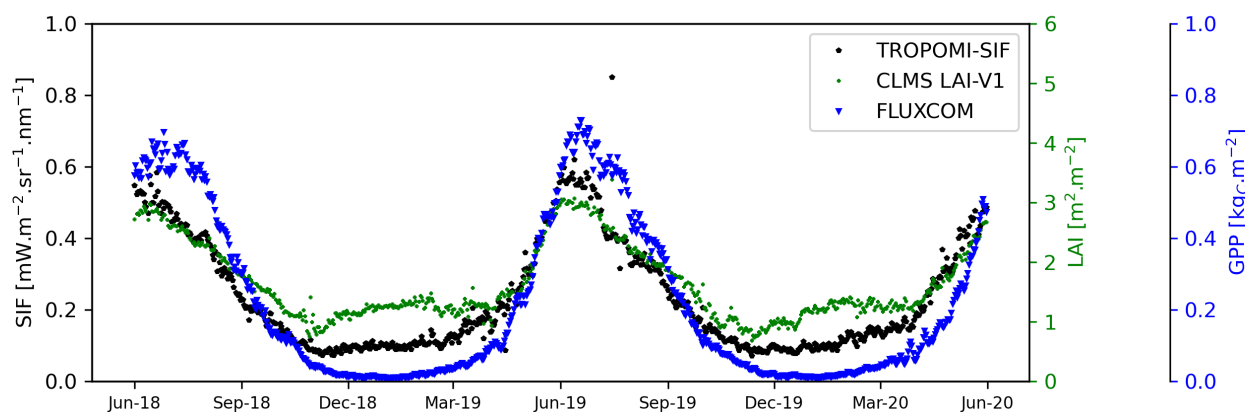


Figure 2. Time series of the median value of LAI (dots), SIF (pentagones) and GPP (inverted triangles) observed over the domain shown in Fig. 1.

For the GPP, we used the most recent global FLUXCOM-X in V0 product (Jung et al., 2020; Nelson et al., 2024). This provides daily estimates of GPP at a quarter-degree resolution across the globe from 2018 to 2021. The time series of the 115 three observation products are displayed in Fig. 2. All of the displayed observations are from the European domain; the GPP



from FLUXCOM remains at its original resolution. The expected seasonal cycle is present in all products. The high-frequency variability in median LAI and TROPOMI SIF values is due to changes in data masking by clouds and filtering applied to both datasets. The isolated spike in mid-July 2019, which is present only in the TROPOMI SIF and LAI V1 datasets, is a rare case in which the Iceland area is the only region observed due to common masking.

120 2.2 Surface modelling and land data assimilation

2.2.1 ISBA land surface model

Throughout this study, we use the version 8.1 of the SURFEX platform (Masson et al., 2013) to model the surface. To model the soil-plant system, we use the ISBA land surface model. Soil moisture and LAI are computed independently for different plant functional types (PFTs). Twelve PFTs are used and distributed according to land use maps. The ISBA model (Noilhan and Planton, 1989; Noilhan and Mahfouf, 1996) is used in the A-gs configuration (Calvet et al., 1998), where A stands for CO₂ assimilation by the leaves and gs stands for the stomatal conductance simulated by the model. ISBA-A-gs considers the functional relationship between stomatal aperture and photosynthesis under well-watered conditions, as described in the biochemical A-gs model proposed by Jacobs (1994); Jacobs et al. (1996). For drier conditions, the model also includes a representation of soil moisture stress, as well as two dedicated drought responses: one for herbaceous vegetation and crops, with specifications for C3 and C4 types (Calvet, 2000), and one for forest vegetation (Calvet et al., 2004). Further details on the ISBA-A-gs can be found in Gibelin et al. (2006). Below the surface, the soil is discretised vertically for both soil temperature and soil moisture. The multi-layer soil model uses a diffusion scheme to solve the one-dimensional Fourier law (Decharme et al., 2011) for soil temperature, and a mixed form of the Richards equation (Richards, 1931) for soil moisture.

2.2.2 Land Data Assimilation system

135 To constrain the ISBA-A-gs model simulations, we assimilate observations sequentially using the global Land Data Assimilation System (LDAS-Monde) described in Albergel et al. (2017). This process involves identifying the optimal control vector according to a model that minimises discrepancies between observations and a prior background estimates. In our case, the control vector comprises the LAI and the soil moisture in the different layers. The results from this process is known as the 'analysis'. We use a simplified extended Kalman filter (SEKF) (Mahfouf and Bilodeau, 2009). Thereafter, the control vector will be referred to as \mathbf{x} , where the subscript denotes the temporal step. The analysis update equation at $t = i$ of the Kalman filter from the background control vector at $t = i - 1$ is as follows:

$$\mathbf{x}_i^b = \mathbf{M}_i(\mathbf{x}_{i-1}^b) \quad (1a)$$

$$\mathbf{x}_i^a = \mathbf{x}_i^b + \mathbf{K}_i(\mathbf{y}_i^o - \mathbf{H}_i(\mathbf{x}_i^b)), \quad (1b)$$

where the superscripts "a", "b", and "o" stand for analysis, background and observation, respectively. The operators \mathbf{M} and \mathbf{H} are respectively the land surface model (i.e. ISBA) and the linear observation operator that maps the control vector into the



observation space. The Kalman gain \mathbf{K}_i is defined at time $t = i$ as follows:

$$\mathbf{K}_i = \mathbf{B}\mathbf{M}_i^\top \mathbf{H}_i^\top (\mathbf{R} + \mathbf{H}_i \mathbf{M}_i \mathbf{B}\mathbf{M}_i^\top \mathbf{H}_i^\top)^{-1}, \quad (2)$$

where \mathbf{B} and \mathbf{R} are error covariance matrices characterizing the background and observation errors. These formulations assume the model and the observation operator to be linear. That is why, in our case we use an extended Kalman filter by using the tangent linear of the operator \mathbf{J} of $\mathbf{H} \circ \mathbf{M}$ instead of its non-linear counterpart. The extended Kalman gain is then defined as follows:

$$\mathbf{x}_i^a = \mathbf{x}_i^b + K_i(\mathbf{y}_i^o - \mathbf{H}_i(\mathbf{x}_i^b)) \quad (3a)$$

$$K_i = \mathbf{B}\mathbf{J}_i^\top (\mathbf{R} + \mathbf{J}_i \mathbf{B}\mathbf{J}_i^\top)^{-1}, \quad (3b)$$

where the tangent linear \mathbf{J} (and his transposed \mathbf{J}^\top), thereafter named Jacobians, are computed using finite differences. This is achieved by perturbing each component of the control vector defined by Rüdiger et al. (2010). To simplify the extended Kalman filter, its background error covariance and the observation error covariance matrices are assumed to be diagonal. These covariance values are fixed for a given assimilation window of 24 hours, as detailed in (Mahfouf et al., 2009; Albergel et al., 2010; Barbu et al., 2011; De Rosnay et al., 2013; Albergel et al., 2017; Fairbairn et al., 2017, among others). The initial state is determined by the analysis performed over the previous 24-hour assimilation window, see Bonan et al. (2020) for more details. The baseline configuration involves assimilating LAI 10-day retrievals with a fixed relative observation error of 20%. Assimilation is assessed when the difference in observation space between the observation and the background simulation exceeds the final departure in the observation space between the observation and the analysis simulation.

2.3 Neural network observation operator

2.3.1 Screening step

For training and evaluation purposes, all areas covered by any fraction of ocean, water, snow or lakes are removed, as are all areas above 1,500 metres above sea level and areas where bare soil, rock, snow or ice are most prevalent according to ECOCLIMAP-II. Grid cells with no LAI or SIF observations, and grid cells where the soil surface temperature fell below 277.15 K according to the SEEDS project analysis (LOBELIA, 2024) and Trimmel et al. (2023), are also excluded to prevent the inclusion of frozen vegetation and soil.

2.3.2 Feed-forward neural network

Here, we address a regression problem that can be solved using a simple feed-forward neural network (NN) for non-linear regression. This strategy produced good results for the assimilation of ASCAT backscattering coefficient σ_0 in Corchia et al. (2023), where the NN was trained on each grid cell independently. However, in this study, we will train a single neural network to cover all pixels. A feed-forward neural network's basic architecture comprises an input layer, one or more hidden layers of neurons, and an output layer, which provides an estimate or probability of belonging to a given category. After some testing, we found that the configuration comprising two hidden layers of 128 ReLu-activated neurons strikes the best balance between



computational cost and accuracy. As our problem is a regression problem, our output layer comprises a single neuron with linear activation as shown in Fig. 3. We added a Gaussian noise layer to the first hidden layer, before the activation layer, to reproduce the effect of a noisy activation layer that would be applied to the inputs. This helps to avoid overfitting during training and enables the duplication of the inputs for data augmentation. This Gaussian layer is only involved during the training process. We expect the neural network to provide smoother estimates than the observations and to filter out the inherent noise of the TROPOMI SIF data. We added a batch normalisation layer at the end of each hidden layer to regularise the learning process.

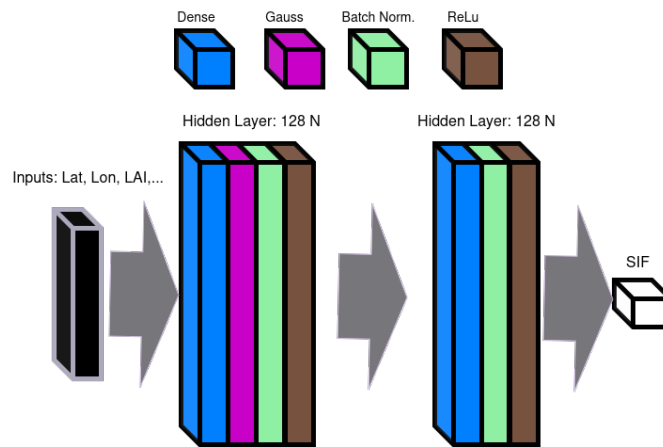


Figure 3. Schematic representation of the neural network architecture

The distribution of TROPOMI SIF values is similar to a log-normal distribution with a maximum close to zero (see in the appendix). To avoid below-zero predictions from the neural network, we applied the following strictly increasing function to the TROPOMI SIF values to predict.

$$SIF_l = \begin{cases} \ln(SIF), & \text{if } SIF \leq 1 \\ \exp(SIF - 1) - 1, & \text{if } SIF > 1. \end{cases} \quad (4a)$$

This analogous function keeps the prediction positive and slightly spreads the distribution. The SIF_l is then used as the output data for the neural network. For the loss function, we compare the label value and the prediction of the neural network according to the Huber loss.

190 2.3.3 Learning process and data split

To gain an insight into the relationship between the TROPOMI SIF data and vegetation-related variables, we calculated the Pearson correlation coefficient between each of the modeled variables and the observations over a one-year period. The variables considered are as follows: GPP, LAI, LAI V1, TROPOMI SIF, surface soil moisture (SSM), evapotranspiration flux (ET) and sensible heat flux, as well as, the latitude (LAT), longitude (LON), day of year (DOY), altitude (ZSE). Ultimately, the LAI-



195 V1 showed the strongest correlation with TROPOMI SIF, even stronger than the modelled LAI from the simulation database. Therefore we will use the observed LAI for the training purposes. Of the simulated variables, only the sensible heat flux and the surface soil moisture are uncorrelated with the SIF estimates. To facilitate the implementation of the LDAS later on, most of the derived variables (i.e. those not in the LDAS control vector) were removed. Only GPP is retained due to its known link to SIF, as well as ET, which is correlated with GPP, LAI and SIF. The remaining candidate inputs belong to one of these three
200 categories:

- control variables of ISBA (i.e. LAI-V1, SSM)
- derived variables of ISBA (i.e. GPP, ET)
- support parameters (i.e. LAT, LON, DOY, ZSE)

However, the results of the training without the DOY, LAT and LON are worse in terms of correlation and mean square error
205 after the initial training experience. These support parameters provide information on the expected seasonal cycles. However, it is questionable whether they will provide information that cannot be changed, which could prevent the model from generalising well on a different grid scale or domain.

To evaluate the importance of each input to the resulting SIF estimate, we calculate the mean Shapley importance value (Lundberg and Lee). This method, which originates from the gaming industry and can be interpreted as a qualitative sensitivity analysis of
210 the resulting SIF estimate with respect to the different inputs. The resulting mean Shapley values are displayed in Fig. 4. The GPP and the ET are the least important inputs, while the LAI, LAT and the DOY have the greatest impact on the estimation. Based on the results of this training test, it has been decided that the ET, GPP, SSM and ZSE inputs can be removed. Unexpect-

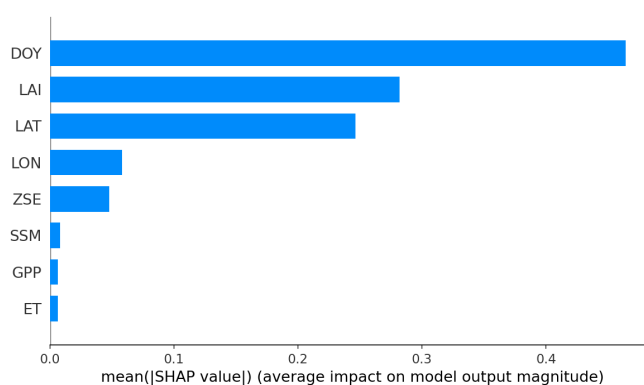


Figure 4. Sensitivity to inputs according to mean Shapley values

edly, the GPP has had almost no impact. This is largely because the LAI already provides most of the necessary information. The final configuration uses only the DOY, LAT, LON and LAI-V1 as predictors. This configuration ensures that, even if the
215 observation operator has learnt the model biases, the assimilation of SIF will not simply adapt to the model and that it will



remain robust to any improvements to the model. The NN was trained for at least 100 epochs to ensure that the 18k weights to estimates had converged. Further details are provided in the appendix.

220 The full data range is from 1 June 2018 to 31 May 2021. The first year is used for the training. Within the training period, 40% of the training database is effectively used for the training of the weights, while the remaining 60% is used to validate the neural network internally during the learning process. This division is randomised to avoid spurious temporal correlations. The 'training' and 'validation' splits are used to check for possible overfitting during training. The test set, which is unknown to the training model, will evaluate the model's ability to generalise. This ranges from 1 June 2019 to 31 May 2020. In summary, the neural network learns using data from one year and is then evaluated using data from a different year. The two evaluation criteria used are the Pearson's correlation coefficient (ρ_p) and the root mean square error (RMSE), as well as the ranges of values.

225

2.4 Assimilation set-up

To limit the computational cost, our focus is on a small area of 40×40 cells within the European domain, where the TROPOMI SIF data will subsequently be assimilated. This domain encompasses the Ebro and Rio Segre basins in Spain. As mention earlier in this study, this area comprises heavily irrigated croplands which are usually not accurately simulated by the land surface model (Jarlan et al., 2023; Lunel et al., 2024). Our approach aims to enhance the simulation of irrigated areas by assimilating TROPOMI SIF data. The assimilation period runs from 1 January 2018 to 31 December 2021 to include the airborne campaign period. The SEKF from the LDAS model assimilates the observations daily at 13:00 UTC. The land cover map used here is defined by ECOCLIMAP-SG (Calvet and Champeaux, 2020), which is more accurate and recent than the land use map ECOCLIMAP-II used to define the training database. The difference from the training map over the Ebro domain are shown in Fig. 1.

230

235

To evaluate the benefits of assimilating TROPOMI SIF data, we will run an open-loop simulation will be conducted from 1 January 2018 onwards. The initial conditions were spun up for 20 years and will be shared by all experiments. The baseline experiment will use the LDAS to assimilate LAI V1 from 1 January 2018 to June 2020. The open-loop simulation will provide a reference point for determining the impact of assimilating SIF data. The baseline experiment will provide a state-of-the-art analysis to evaluate the specific benefits of assimilating SIF data. To determine the amount of observation error to consider, three different experiments will be run with three different amounts of error: (i) $0.1 \text{ mW.m}^{-2}.\text{sr}^{-1}.\text{nm}^{-1}$, (ii) 20% of relative error, and (iii) a combination of the previous two errors with a fixed error of $0.1 \text{ mW.m}^{-2}.\text{sr}^{-1}.\text{nm}^{-1}$ for SIF values below $0.5 \text{ mW.m}^{-2}.\text{sr}^{-1}.\text{nm}^{-1}$ and 20% of relative error for values above $0.5 \text{ mW.m}^{-2}.\text{sr}^{-1}.\text{nm}^{-1}$. This configuration will be denoted *FR* thereafter. Two additional experiment will be run to test the co-assimilation of TROPOMI SIF and CLMS LAI 300 m raster for two different values of the SIF observation error and 20% of relative error for the LAI (Barbu et al., 2011). All experiment configurations are summarised in Table 1.

240

245



Table 1. Overview of the assimilation experiments conducted for TROPOMI SIF. The table indicates the name of the assimilation experiment (Experiment name), the assimilation of the LAI and which dataset (LAI) with an observation error of 20%, the assimilation of TROPOMI SIF (SIF) with which observation error (σ) used.

Experiment name	LAI ($\text{m}^2 \cdot \text{m}^{-2}$)		SIF ($\text{mW} \cdot \text{m}^{-2} \cdot \text{sr}^{-1} \cdot \text{nm}^{-1}$)		
	LAI V1	LAI 300	$\sigma = 0.1$	$\sigma = 20\%$	FR
OL	-	-	-	-	-
LAI_V1	X	-	-	-	-
SIF ₀₁	-	-	X	-	-
SIF ₂₀	-	-	-	X	-
SIF _{FR}	-	-	-	-	X
SL ₂₀	-	X	-	X	-
SL _{FR}	-	X	-	-	X

3 Results

3.1 Validation of the observation operator

The correlation between TROPOMI SIF and the estimate from the operator is above 0.8 and the RMSE on SIF is around 0.15 $\text{mWm}^{-2} \cdot \text{sr}^{-1} \cdot \text{nm}^{-1}$ as displayed in Table 2. However, the neural network's range is smaller than that of the TROPOMI SIF. Both the values closest to and farthest from zero are miss-estimated by the NN. To improve our understanding of the neural network's behaviour, we evaluate its performance on specific TROPOMI SIF samples. We also check whether the neural network's behaviour is sensitive to the range of TROPOMI SIF values and the dominant PFT, in order to ascertain whether it learns features relating to vegetation distribution and phenology. Table 2 shows the results for both the training and test datasets to detect any overfitting.

As shown in Table 2, the values based on the training and test datasets are in good agreement. This suggests that if there is any overfitting, it is limited. Comparing the skill scores for the different percentiles of TROPOMI SIF values, we can see that, as we consider more data from the edges of the distribution, the bias, the RMSE and the correlation all increase. This indicates that the neural network disregards minor variations around the mean TROPOMI SIF value. This behaviour is to be expected due to the use of Huber loss during training, which focuses on minimising the RMSE. Furthermore, when the values are farther from the mean, the neural network follows this change, thereby increasing the correlation. However, the bias also increases with the SIF value, thus increasing the RMSE.

A negative bias means that the neural network is underestimating the TROPOMI SIF value. This is particularly evident for the largest SIF values. The neural network performs better over areas where crops, grasslands and deciduous broadleaf forests are most prevalent. Coniferous needle-leaf forests (CNF) and flooded areas (irrigated crops) seem to present more difficulty, as Table 2 shows.



Table 2. Evaluation of the neural network over the train and the test dataset (Train/Test). The percentiles are taken from the range of TROPOMI SIF values. RMSE and ubRMSE are given in $\text{mW}\cdot\text{m}^{-2}\cdot\text{sr}^{-1}\cdot\text{nm}^{-1}$

Train/Test dataset Score	RMSE	ρ_p	Bias (NN-Obs)	ubRMSE	Median (NN-Obs)	Min (NN-Obs)	Max (NN-Obs)	Dataset size
Percentile [25,75]	0.11/0.12	0.56/0.53	-0.004/-0.008	0.11/0.12	-0.02/-0.02	-0.40/-0.43	1.82/1.79	7,156,450/7,011,925
Percentile [10,90]	0.12/0.12	0.74/0.73	-0.01/-0.02	0.11/0.12	-0.02/-0.02	-0.60/-0.64	1.82/1.79	11,450,319/11,219,078
Percentile [5,95]	0.12/0.13	0.79/0.77	-0.02/-0.02	0.12/0.13	-0.01/-0.02	-0.71/-0.76	1.82/1.79	12,881,610/12,621,462
Percentile[1,99]	0.13/0.14	0.81/0.81	-0.02/-0.03	0.13/0.14	-0.01/-0.02	-0.94/-0.98	1.82/1.79	14,026,641/13,743,370
All	0.14/0.15	0.82/0.81	-0.03/-0.03	0.14/0.15	-0.01/-0.02	-3.59/-3.82	1.82/1.79	14,312,899/14,023,848
Deciduous Broadleaves Forest	0.15/0.17	0.82/0.80	-0.03/-0.03	0.15/0.16	-0.02/-0.02	-3.44/-3.82	1.57/1.74	1,542,837/1,319,870
Coniferous Needleleaves Forest	0.13/0.15	0.71/0.65	$-5 \times 10^{-3}/-7 \times 10^{-3}$	0.13/0.15	0.0/0.0	-3.59/-3.64	1.82/1.79	1,897,962/1,667,631
Evergreen Broadleaves Forest	-/-	-/-	-/-	-/-	-/-	-/-	-/-	0/0
C3 crops	0.14/0.15	0.84/0.83	-0.04/-0.05	0.13/0.14	-0.02/-0.03	-3.55/-3.45	1.28/1.55	5,730,186/5,804,070
C4 crops	0.14/0.14	0.87/0.87	-0.04/-0.05	0.13/0.13	-0.02/-0.03	-2.81/-2.78	0.67/0.75	207,755/222,823
Irrigated Crops	0.15/0.14	0.77/0.77	-0.05/-0.04	0.14/0.14	-0.03/-0.03	-1.25/-1.41	0.60/0.67	102,170/107,158
C3 grasslands	0.14/0.15	0.82/0.82	-0.02/-0.03	0.14/0.15	-0.007/-0.014	-3.34/-3.26	1.23/1.33	4,617,598/4,716,617
C4 grasslands	-/-	-/-	-/-	-/-	-/-	-/-	-/-	0/0
Peats and Wetlands	0.16/0.17	0.82/0.78	-0.04/-0.04	0.16/0.17	-0.02/-0.02	-2.67/-2.89	1.53/1.37	214,391/185,679

The differences in behaviour depending on the SIF values and the PFT motivate us to verify whether some spatial properties need to be considered in our evaluation. Figure 5 shows the local values of the root mean square error (RMSE), correlation, number of available comparisons and normalised root mean square error (NRMSE) for the entire test dataset. The normalisation is done by the TROPOMI SIF value. The correlation is above 0.8 in the area south of 60°N . This is due to the number of observations available in the region. The northern area is not observed for more than half of the year by TROPOMI around the winter period and less LAI observation are available.

Based on the spatial distribution of observations over the course of a year, we can expect approximately one observation every two days. The RMSE is heterogeneously distributed, highlighting the known areas of C3 crops, and ranges between 0.1 and 0.2 $\text{mW}\cdot\text{m}^{-2}\cdot\text{sr}^{-1}\cdot\text{nm}^{-1}$. The NRMSE distribution is more uniform than the RMSE distribution, averaging at around 20%. Underestimation appears to be proportional to the values of TROPOMI SIF, so considering a fixed value for the observation error seems inaccurate. That is why, we tested different observation errors.

3.2 Assimilation in the Ebro basin

The saved weights of the neural network are implemented in the assimilation scheme as an observation operator for the SIF. The LAI is simulated and used as input data. In this case, the NN is only used in forward mode and the weights will not change. As the observation operator only takes LAI as inputs, LAI representation will be our main focus on the control vector variables. The LAI increments are significant, reaching up to $0.2 \text{ m}\cdot\text{m}^{-2}$, as shown by the monthly-averaged maps over the C3 crops (Fig. 6). The residuals, the remaining differences between the analysed SIF and the observed SIF, are smaller than the innovation vectors, the difference between modeled SIF and observed SIF. This illustrates that the assimilation of SIF leads to the identification of such observed agricultural practices in the model, even when they are not simulated. Here, we observe

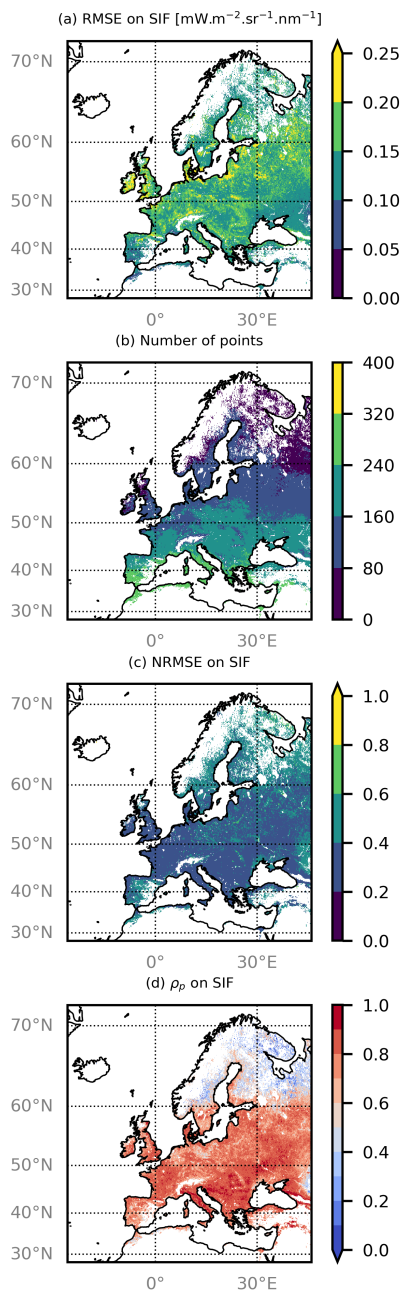


Figure 5. Grid-pointwise evaluation of the performance of the match between NN and observations for the test dataset. From top to bottom: the RMSE, the number of comparison per pixels, the NRMSE, and the Pearson correlation. Units are indicated were applicable.

a confined area around the Ebro basin where LAI increased during the summer of 2021. This pattern was also evident in the other years of the experiment. This confined area is artificially irrigated (Ricart et al., 2016). Irrigation sustains the LAI and

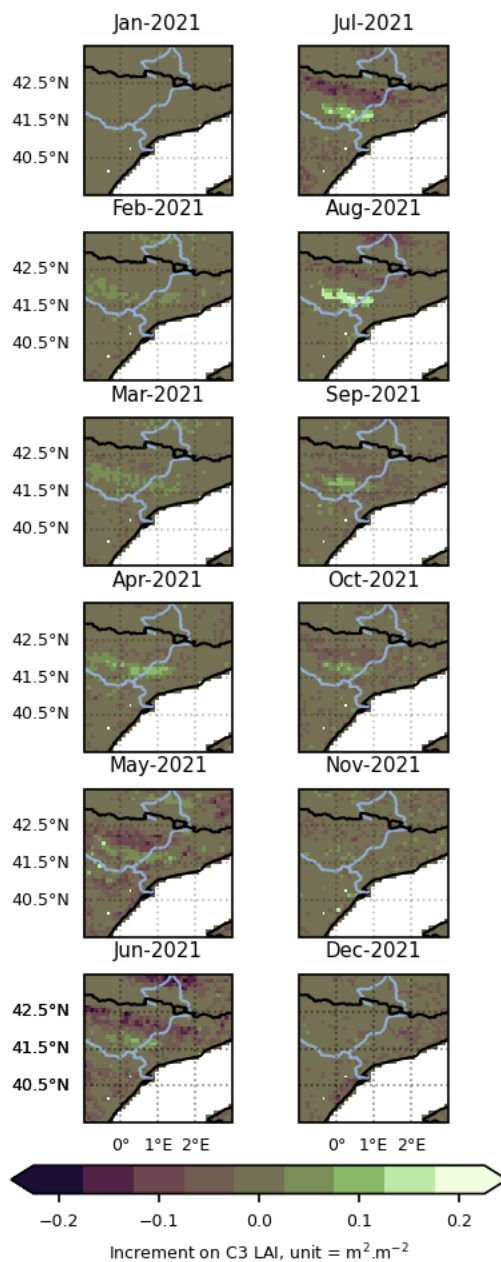


Figure 6. Mean monthly analysis increments on the LAI of C3 crops due to SIF assimilation during the year 2021.

SIF, while other areas become drier. This illustrates that the assimilation of SIF leads to the identification of such observed agricultural practices in the model, even when they are not simulated. This positively impacts on the representation of LAI, as
290 demonstrated by the map of the differences between the RMSEs in Fig. 7. The difference is computed so that negative values



result from a lower RMSE in the analysis than in the open-loop experiment and are displayed with a lighter color. TROPOMI SIF assimilation tends to decrease the RMSE for LAI, using LAI-V1 as a reference (until June 2020). This decrease in RMSE occurs almost everywhere, particularly over deciduous broadleaf forests. During the same period, we calculated the difference in correlation with respect to the 10-day LAI-V1 product between the open-loop experiment and the analysis. The resulting map is displayed in Fig. 7. As only one observation is available every 10 days for calculating the correlation, all cells with a p-value higher than 0.01 were removed. The assimilation of TROPOMI SIF provides mixed results regarding the correlation with LAI. There are small dark patches where the correlation decreases in southern Spain, but the correlations of the croplands area are improved.

For the irrigated pixels in question, which correspond to the areas where field measurements were taken and marked with a cross in Fig. 7, the estimates of SIF and LAI from the analysis are closer to the observed values. Correction of the GPP is less significant, however, assimilating SIF improves the correlation with the FLUXCOM-GPP as shown in the boxplots displayed in Fig. 8. This shows that, on average, assimilating SIF provides a similarly accurate representation of GPP than assimilating CLMS LAI-V1.

3.2.1 Evaluation of the observation error

The time series showing the differences between the averaged RMSE from the different analyses and the one from the open-loop RMSE are displayed in Fig. 9. The RMSE for SIF₂₀ analysis tends to match the RMSE from the reference LAI-V1 experiment and is sometimes even lower. In the case of SIF₀₁ and SIF_{FR}, the RMSE is close to that of the open-loop experiment, even though the SIF_{FR} configuration provide a better RMSE on LAI than the SIF₀₁ configuration. This suggests that our first guess (i.e. 20% of relative error) in terms of observation error is close to the optimal situation for minimising the RMSE, and that higher values tend to render assimilation ineffective.

3.2.2 Co-assimilation of LAI and SIF

When it comes to data assimilation, the question of redundancy in observations is important, since disagreement between observations can degrade the analysis, while agreement can improve it further. Two configurations of co-assimilation, SL₂₀ and SL_{FR} of the LAI-300 from CLMS and the TROPOMI SIF are run on the Ebro basin domain. We compare the RMSE on LAI for each cell of the assimilation domain averaged from June 2018 to May 2020 for all assimilation experiments and display the results in Fig. 10. This co-assimilation configuration achieves an RMSE that is at least as good as that achieved by assimilating either LAI or SIF alone.

As mentioned earlier, the assimilation of TROPOMI SIF as the only observations should be done with a relative error of 20% to achieve the greatest decrease in RMSE. When compared with the analysis resulting from the assimilation of the CLMS 10-day LAI-V1 synthesis, the average RMSE is lower when assimilating LAI than when assimilating SIF only, but by a small margin for the SIF₂₀ experiment. In both cases of co-assimilation, co-assimilating SIF alongside LAI achieves better results than assimilating only LAI-V1 or TROPOMI SIF, regardless of the observation error on TROPOMI SIF. Furthermore, the FR configuration in co-assimilation does not degrade the results as much as when only TROPOMI SIF is assimilated, providing

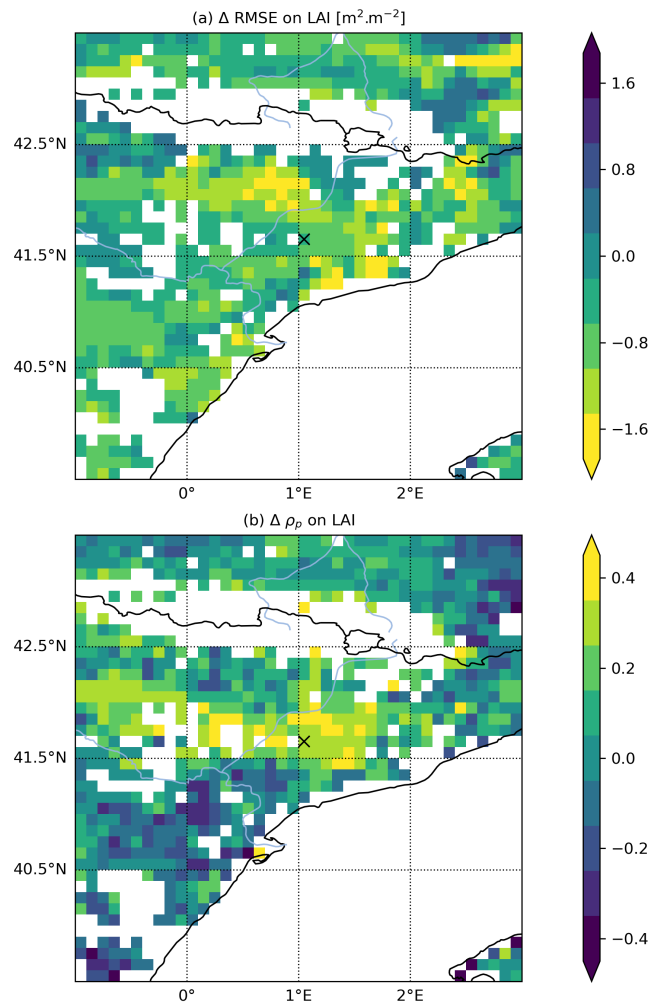


Figure 7. Differences (SIF₂₀ -OL) in (a) RMSE and (b) ρ_p computed with respect to LAI observations after and before assimilation of SIF averaged from June 2018 to May 2020. (a) Δ RMSE between the OL and the analysis. (b) $\Delta \rho_p$ on LAI. The cross marks the location of the HyPlant campaign

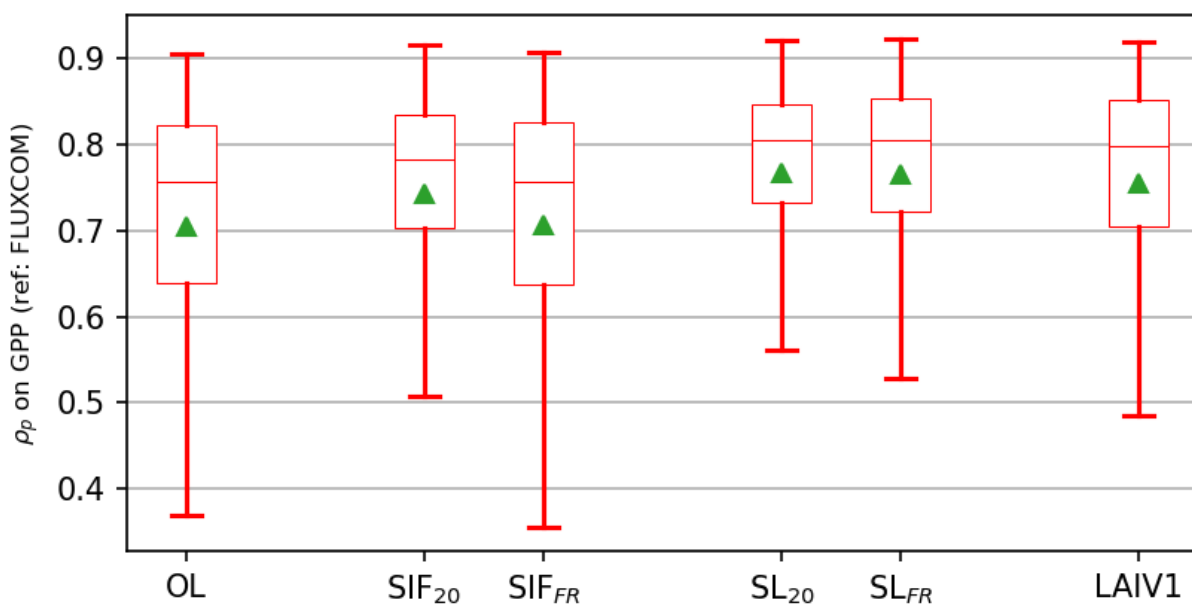


Figure 8. Box plot of the correlation between analysis, open-loop simulated GPP and the FLUXCOM dataset. From left to right: Open-loop, SIF₂₀, SIF_{FR}, Coassimilation SL₂₀ and SL_{FR} configurations and assimilation of LAI-V1. The boxes represent the 25th and the 75th percentiles, the whiskers the 5th and 95th percentiles. The red line represents the 50th percentile and the green triangle the mean.

a more consistent improvement than the SL₂₀ analysis. This demonstrates that co-assimilation of TROPOMI SIF with a 10-
325 day LAI product improves the LAI representation further. The key finding is that the assimilation of TROPOMI SIF leads to changes in the day-to-day monitoring of fluxes and LAI. This results in more accurate trends and better agreement with observations of LAI and GPP than assimilation of the LAI product alone as illustrates in Fig. 8.

4 Discussion

4.1 Does the neural network works as a SIF model?

330 The initial purpose of the neural network observation operator was to enable the assimilation of TROPOMI SIF retrieval. To achieve this, the operator was initially trained to mimic TROPOMI SIF retrieval using the LDAS control variables. Here, we discuss whether the neural network should be used solely as an observation operator, or whether the SIF simulation obtained through the operator can agree with SIF observations. We compare the daily SIF values retrieved from the open-loop experiment and the SIF₂₀ experiment for the selected grid cell located with the 10-m resolution airborne measurements from the
335 HyPlant campaign and with the TROPOMI SIF values. As the in-situ observations and the TROPOMI-SIF are centred on different wavelengths, we will focus more on the temporal variations than the actual values of the simulated SIF. The significant

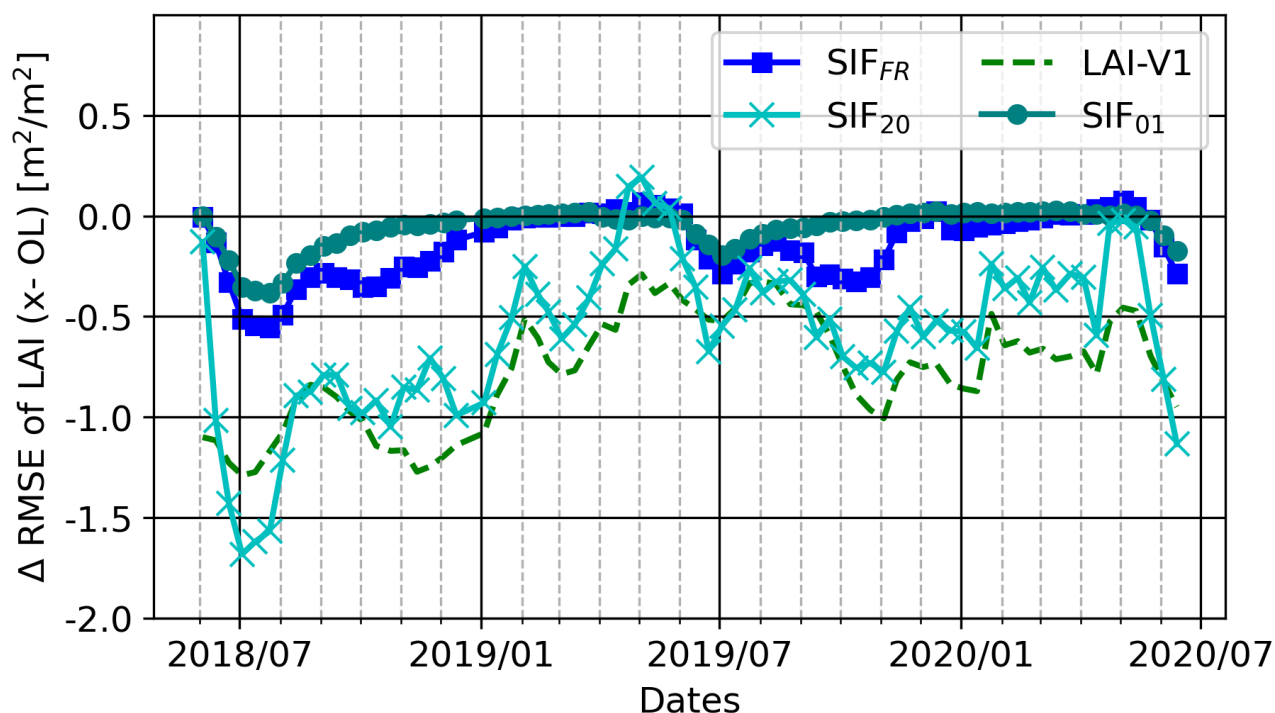


Figure 9. Δ RMSE between the Open-Loop and the LAI analysis of the assimilation experiments from January 2018 to January 2020.

difference in spatial resolution means that we must compare all in-situ SIF measurements on a given day with the simulated SIF value resulting from the analysis for the two situations shown in Fig. 11(b). For the two SIF simulations resulting from the analysis and the open-loop experiment, we use the average LAI value for all PFTs to compute the SIF with the neural network.

340 Comparing the results with those of the open-loop experiment reveals that when TROPOMI SIF is assimilated, the values are closer overall to the average airborne measurement value, though they do not follow the airborne daily average variations. As expected, the simulated SIF values are closer to the TROPOMI SIF values in terms of both magnitude and temporal variation than the airborne measurement average, since the neural network was trained to match the TROPOMI SIF retrieval. This is an example of the limitations of using a neural network. Although the neural network was trained using observations, which

345 means it is independent of the LSM used for assimilation, this does not make it an emulator of any SIF observation.

4.2 Does the GPP require additional observations to be better constrained?

Unexpectedly, the GPP seems to benefit less from SIF assimilation, even though SIF is known to be well correlated with the GPP. While the GPP is improved on average across the domain by assimilating SIF, the local comparison displayed in Fig. 12 shows that it is difficult for the analysed GPP to be significantly improved. This result stems from the way the GPP

350 is modelled by the ISBA LSM. The modelled GPP depends not only on the vegetation parameter, but also on the soil water

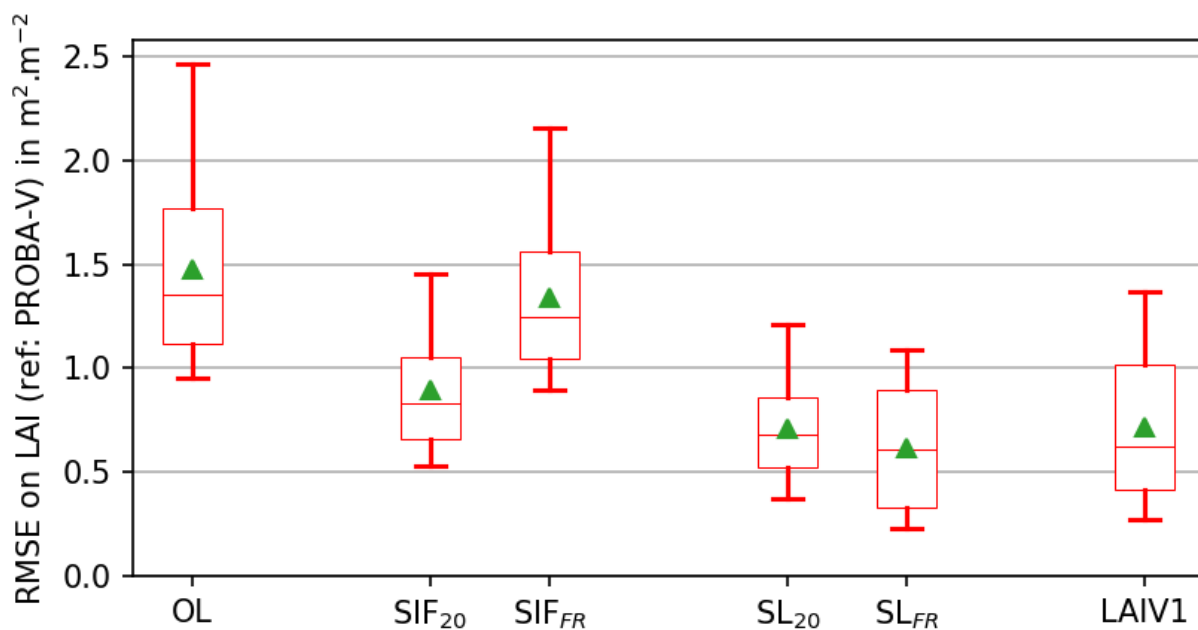


Figure 10. Boxplot of the RMSE for the different LAI predictions taken between June 2018 and June 2020. Box represents the 25th and the 75th percentiles, the whiskers the 5th and 95th percentiles. The red line represents the 50th percentile and the green triangle the mean.

content. Assimilating SIF often results in a more accurate representation of LAI, and in our local case, it adds more LAI in summer than the open-loop model forecasts. This increase in LAI causes the model soil to dry out. Consequently, unlike its observed counterpart, which is the result of irrigating the field, the computed GPP cannot increase. Thus, assimilating SIF yields the same results as assimilating LAI directly from the GPP perspective. As such, assimilating SIF corrects the LAI and updates the soil water content in order to balance the change in LAI. However, it cannot infer an increase in soil water content, which would make the model's GPP more similar to the FLUXCOM estimate.

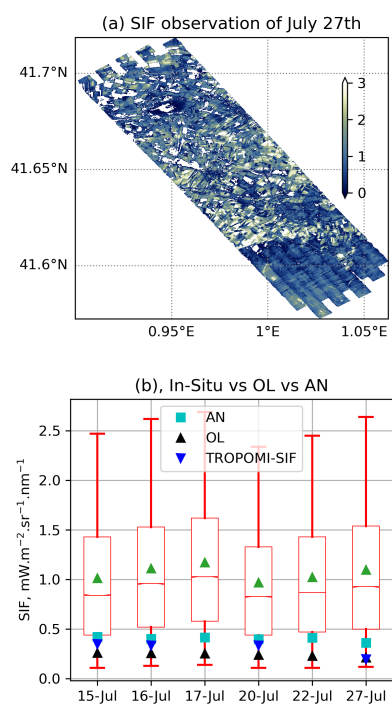


Figure 11. Comparison to the in-situ measurements of SIF during the LIAISE campaign (OL: Open-loop, AN: analysis). Box represents the 25th and the 75th percentiles, the whiskers the 5th and 95th percentiles. The red line represents the 50th percentile and the green triangle the mean.

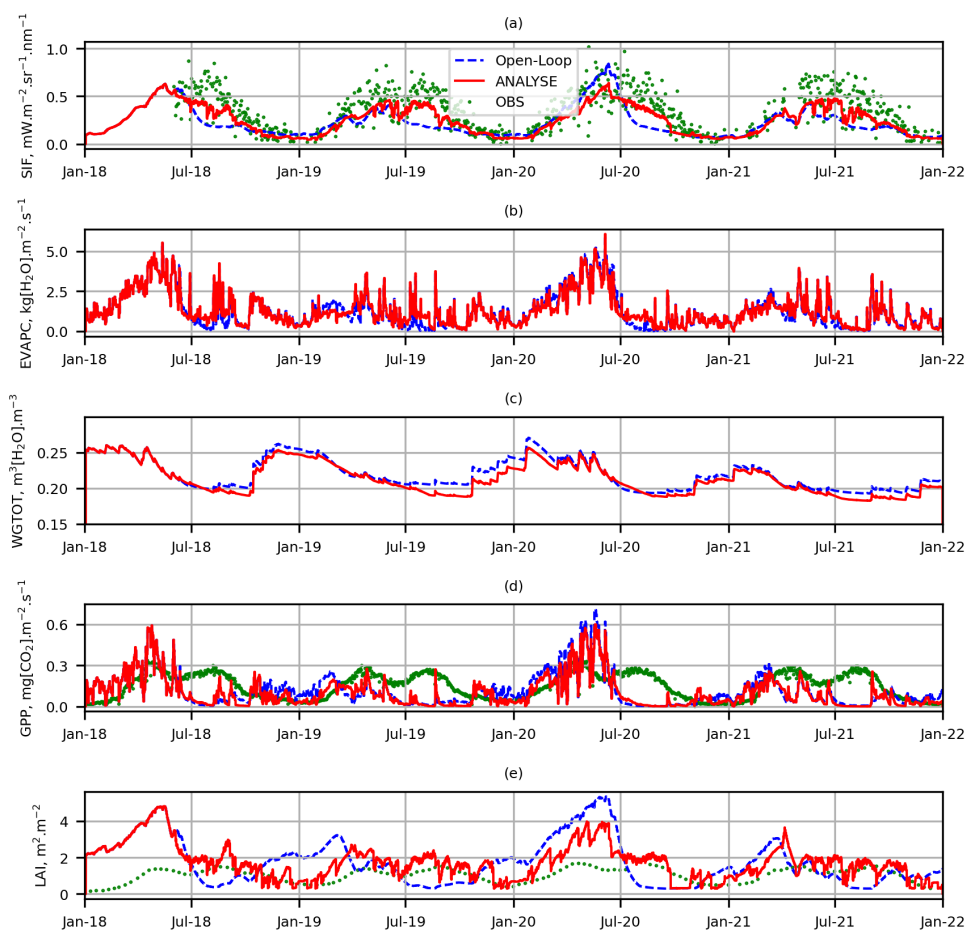


Figure 12. Timeseries extract on the cell locate in 1.05°E, 41.65°N for the SIF, the cumulated evapotranspiration, the total column water content, the GPP, and the LAI. The open loop is indicated with dashed blue lines, analysis with the plain red line and observations with green dots. The observations for the SIF, LAI, and GPP are respectively extracted from TROPOMI SIF, FLUXCOM and LAI databases described in section 2.2.3



5 Conclusion

In this article, we examined the use of a deep learning emulator of TROPOMI SIF as an observation operator, and explored the advantages of incorporating TROPOMI SIF into a land surface model with this observation operator. The neural network operator takes the LAI and three support parameters as inputs: the two geographical coordinates and the day of the year. Using this simple architecture, we achieved an average RMSE of $0.15 \text{ mW}\cdot\text{m}^{-2}\cdot\text{sr}^{-1}\cdot\text{nm}^{-1}$ on the TROPOMI SIF averaged estimate, with no overfitting evident. The neural network was then successfully used as an observation operator considering an observation error relative to the average TROPOMI SIF value. The Pearson correlation coefficient between the neural network estimate and TROPOMI SIF is greater than 0.8, with higher correlations observed in cropland areas than in coniferous areas. However, the neural network struggles with statistically extreme values, which increases the averaged RMSE and introduces bias. It is also unable to capture small variations close to the expected mean value. Nevertheless, it does capture significant changes in the TROPOMI SIF, such as those due to the changing seasons.

Several assimilation experiments were conducted over an irrigated cropland area in the Ebro basin. TROPOMI SIF assimilation had a similar positive impact on LAI as the assimilation of the 10-day LAI observation product. However, it should be noted that the update rate yielded by TROPOMI SIF assimilation is five times higher than that of 10-day synthesis assimilation. Despite not being predicted by the LSM or provided as inputs to the neural network, irrigated areas are well represented. The analysis also led to improved representations of TROPOMI SIF and of changes in GPP, both of which are important for monitoring the carbon cycle.

Using a neural network operator instead of a physical model makes propagating uncertainties difficult, so quantifying observation errors relies more on empirical choices. It is also important to understand that the neural network is trained to emulate observations with instrument uncertainties rather than the true physical variable, making quantifying the observation error of the true value challenging. While the usual diagnostic of observation errors may suggest using a larger error, this would suppress the positive impact of TROPOMI assimilation. A dedicated study must be conducted on a global scale to quantify the amount of error to be used. While using an observation error that scales with SIF values provides better results, good results can be achieved by applying a compound definition of observation error. Co-assimilating LAI and TROPOMI SIF yields even better results, demonstrating the value of redundancy in observations used in a data assimilation system.

This study assesses the benefits of incorporating TROPOMI SIF products into a land data assimilation system via a deep learning operator, which opens up new possibilities for systematically assimilating such products. As the architecture and training of the neural network operator are not overly specific to the TROPOMI SIF product, it would be interesting to adapt it for the assimilation of other SIF products. Better optimisation of the hyperparameters or the use of additional variables could enhance the neural network's accuracy.

Code and data availability. The final weights computed for the neural-network, the database used for training are stored in zenodo repository <https://doi.org/10.5281/zenodo.18669437>. The simulations and different analysis resulting from SIF assimilation are available in zenodo

repository <https://doi.org/10.5281/zenodo.18668100>. The Hyplant raw measurements are available through LIAISE data portal <https://liaise.aeris-390 data.fr/about/>

Appendix A: Details on the Neural Network

A1 Choice of the output

The neural network tends to perform better with normalised data and with distribution close to a Gaussian. After filtering, the distribution of SIF measurements ends up being log-normal like with a maximum close to 0 as Fig. A1(a) shows. To make the
395 distribution more Gaussian like, and thus ease the training of the NN, we applied the function Eq. (4). The distribution of the transformed values SIF_t is displayed in Fig. A1(b). One can notice that the function is easily reversed to recover the true value of SIF.

A2 Choice of the inputs

The SIF signal is produced under specific conditions during the photosynthesis process (Rossini et al., 2015). Its magnitude
400 is correlated with environmental conditions such as the hydrological stress experienced by vegetation (Sun et al., 2015). On a larger scale, this results in an almost linear relation between the SIF signal, the LAI, and the GPP. However, the slope of this relationship is sensitive to the vegetation type, the regional climate, and the season (Leroux et al., 2018). We considered the following predictors: the day of the year (DOY), the latitude (LAT) and the longitude (LON), the surface elevation (ALT), the surface soil moisture (SSM), the land surface temperature (LST), the net radiative flux (RNF), the evapotranspiration
405 (ET), the latent heat flux (H), the GPP, and the LAI as well as the 10-day average LAI_V1. To obtain an initial estimate on the relationship between these variables and the TROPOMI-SIF data, we compute Pearson's correlation coefficient for each variable over a one-year period (Fig. A2).

The LAI_GEOV1 shows the strongest correlation with TROPOMI-SIF. Of the simulated variables, only the latent heat flux and the surface soil moisture are uncorrelated with the SIF estimates. These are therefore eliminated from the suitable inputs
410 for the neural network. Thus the remaining candidate inputs considered belong to one of these three categories:

- control variables of ISBA (i.e. LAI, SSM)
- derived variables of ISBA (i.e. GPP, ET, RNF, LST)
- support parameters (i.e. LAT, LON, DOY, ALT)

TROPOMI-SIF is uncorrelated with all the support parameters. However, after initial training experience, the results of the
415 training without the DOY, LAT and LON are worse in terms of correlation and mean square error. These support parameters provide information on the expected seasonal cycles. Yet, their use is questionable since they will provide information that cannot be changed, which could prevent the model from generalising well.



Keeping all the derived variables only improves the training results slightly, and the Shapley values show that they are not significant in the SIF emulation by the NN. Using the GPP as input also does not seem to have a significant impact. This is mostly because the LAI yields most of the information. The objective here is not to reproduce the TROPOMI-SIF signal perfectly, but rather to design an operator that strikes a balance between the accuracy of the estimated TROPOMI-SIF observation, ease the use within our data assimilation framework, and significant impact on the analysis. The derived variables complicate the assimilation scheme by involving prognostic variables and diagnostic variables from the model. This leads us to discard these categories of predictors.

425 **A3 Learning process details**

Due to regularisation, the validation loss tends to be lower than the training loss. However, as the Fig. A3 shows, both converge. We compare the learning curves in terms of both the Huber loss applied to ϕ and the mean square error on the SIF estimation reconstructed from ϕ . The reconstructed mean squared error appears to be more variable, but remains low. A learning scheduler was used for the training, the learning rate dropped every 20 epochs by 0.5 power of the floor part of the number of epochs completed so far divided by 20 every 20 epochs. This ranges from 0.001 for the first twenty epochs to 1×10^{-6} for the last twenty. This results in the large steps in the learning curves displayed in Fig. A3.

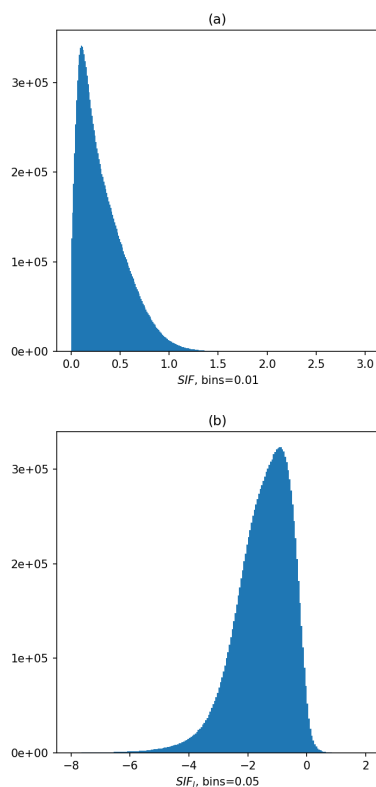


Figure A1. Comparison of the distribution of the SIF values from both the train and the test period and the analog ϕ values used for the neural network.

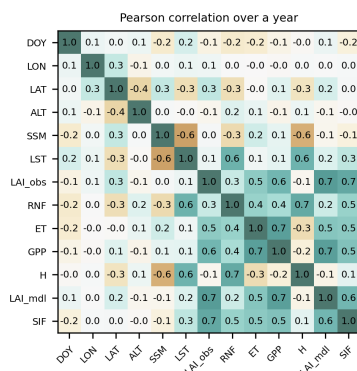


Figure A2. Pearson's correlation between potentially suitable inputs.

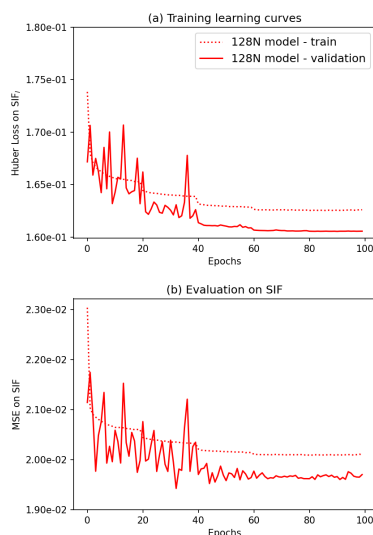


Figure A3. Learning curves of the neural-network over the SEEDS domain.

Author contributions. PV conducted the investigation and analysed the data, writing the article under the supervision of JCC. JV, BB and ORM helped with the development of the methodology and software. JV, BB, ORM, SG also helped PV validate the results. JCC and PdR administered the project, while CB provided useful advice on the TROPOSIF dataset and UR and BS provided the Hyplant dataset. All co-authors reviewed the article.

Competing interests. None

Acknowledgements. This research received funding from European Union Horizon Europe through CORSO project (grant agreement 101082194) and CERISE project (grant agreement 101082139). Views and opinions expressed are those of the authors only and do not necessarily reflect those of the European Union or the Commission. Neither the European Union nor the granting authority can be held responsible for them. The comparison with in situ SIF observation was possible thanks to the HyPlant field campaign fund by CNES.



References

- Agustí-Panareda, A., McNorton, J., Balsamo, G., Baier, B. C., Bousserez, N., Boussetta, S., Brunner, D., Chevallier, F., Choulga, M., Diamantakis, M., et al.: Global nature run data with realistic high-resolution carbon weather for the year of the Paris agreement, *Scientific Data*, 9, 160, 2022.
- 445 Albergel, C., Calvet, J.-C., Mahfouf, J.-F., Rüdiger, C., Barbu, A., Lafont, S., Roujean, J.-L., Walker, J., Crapeau, M., and Wigneron, J.-P.: Monitoring of water and carbon fluxes using a land data assimilation system: a case study for southwestern France, *Hydrology and Earth System Sciences*, 14, 1109–1124, 2010.
- Albergel, C., Munier, S., Leroux, D. J., Dewaele, H., Fairbairn, D., Barbu, A. L., Gelati, E., Dorigo, W., Faroux, S., Meurey, C., Le Moigne, P., Decharme, B., Mahfouf, J.-F., and Calvet, J.-C.: Sequential assimilation of satellite-derived vegetation and soil moisture products using SURFEX_v8.0: LDAS-Monde assessment over the Euro-Mediterranean area, *Geoscientific Model Development*, 10, 3889–3912, <https://doi.org/10.5194/gmd-10-3889-2017>, 2017.
- 450 Albergel, C., Zheng, Y., Bonan, B., Dutra, E., Rodríguez-Fernández, N., Munier, S., Draper, C., de Rosnay, P., Muñoz Sabater, J., Balsamo, G., Fairbairn, D., Meurey, C., and Calvet, J.-C.: Data assimilation for continuous global assessment of severe conditions over terrestrial surfaces, *Hydrology and Earth System Sciences*, 24, 4291–4316, <https://doi.org/10.5194/hess-24-4291-2020>, 2020.
- 455 Bacour, C., Maignan, F., MacBean, N., Porcar-Castell, A., Flexas, J., Frankenberg, C., Peylin, P., Chevallier, F., Vuichard, N., and Bastrikov, V.: Improving Estimates of Gross Primary Productivity by Assimilating Solar-Induced Fluorescence Satellite Retrievals in a Terrestrial Biosphere Model Using a Process-Based SIF Model, *Journal of Geophysical Research: Biogeosciences*, 124, 3281–3306, <https://doi.org/https://doi.org/10.1029/2019JG005040>, 2019.
- Barbu, A., Calvet, J.-C., Mahfouf, J.-F., Albergel, C., and Lafont, S.: Assimilation of Soil Wetness Index and Leaf Area Index into the ISBA-A-gs land surface model: grassland case study, *Biogeosciences*, 8, 1971–1986, 2011.
- 460 Berry, J.: 3.10 solar induced chlorophyll fluorescence: Origins, relation to photosynthesis and retrieval, *Compr. Remote Sens*, 3, 143–162, 2018.
- Bolhar-Nordenkamp, H. R., Long, S. P., Baker, N. R., Oquist, G., Schreiber, U., and Lechner, E. G.: Chlorophyll Fluorescence as a Probe of the Photosynthetic Competence of Leaves in the Field: A Review of Current Instrumentation, *Functional Ecology*, 3, 497–514, <http://www.jstor.org/stable/2389624>, 1989.
- 465 Bonan, B., Albergel, C., Zheng, Y., Barbu, A. L., Fairbairn, D., Munier, S., and Calvet, J.-C.: An ensemble square root filter for the joint assimilation of surface soil moisture and leaf area index within the Land Data Assimilation System LDAS-Monde: application over the Euro-Mediterranean region, *Hydrology and Earth System Sciences*, 24, 325–347, <https://doi.org/10.5194/hess-24-325-2020>, 2020.
- Butterfield, Z., Magney, T., Grossmann, K., Bohrer, G., Vogel, C., Barr, S., and Keppel-Aleks, G.: Accounting for changes in radiation improves the ability of SIF to track water stress-induced losses in summer GPP in a temperate deciduous forest, *Journal of Geophysical Research: Biogeosciences*, 128, e2022JG007352, 2023.
- 470 Calvet, J.-C.: Investigating soil and atmospheric plant water stress using physiological and micrometeorological data, *Agricultural and Forest Meteorology*, 103, 229–247, 2000.
- Calvet, J.-C. and Champeaux, J.-L.: L'apport de la télédétection spatiale à la modélisation des surfaces continentales, *La Météorologie*, 108, 52–58, <https://doi.org/10.37053/lameteorologie-2020-0016>, 2020.
- 475 Calvet, J.-C., Noilhan, J., Roujean, J.-L., Bessemoulin, P., Cabelguenne, M., Olioso, A., and Wigneron, J.-P.: An interactive vegetation SVAT model tested against data from six contrasting sites, *Agricultural and Forest Meteorology*, 92, 73–95, 1998.



- Calvet, J.-C., Rivalland, V., Picon-Cochard, C., and Guehl, J.-M.: Modelling forest transpiration and CO₂ fluxes—Response to soil moisture stress, *Agricultural and forest meteorology*, 124, 143–156, 2004.
- 480 Corchia, T., Bonan, B., Rodríguez-Fernández, N., Colas, G., and Calvet, J.-C.: Assimilation of ASCAT Radar Backscatter Coefficients over Southwestern France, *Remote Sensing*, 15, 4258, 2023.
- De Rosnay, P., Drusch, M., Vasiljevic, D., Balsamo, G., Albergel, C., and Isaksen, L.: A simplified extended Kalman filter for the global operational soil moisture analysis at ECMWF, *Quarterly Journal of the Royal Meteorological Society*, 139, 1199–1213, 2013.
- Decharme, B., Boone, A., Delire, C., and Noilhan, J.: Local evaluation of the Interaction between Soil Biosphere Atmosphere soil multilayer
485 diffusion scheme using four pedotransfer functions, *Journal of Geophysical Research: Atmospheres*, 116, 2011.
- Decharme, B., Martin, E., and Faroux, S.: Reconciling soil thermal and hydrological lower boundary conditions in land surface models, *Journal of Geophysical Research: Atmospheres*, 118, 7819–7834, 2013.
- Fairbairn, D., Barbu, A. L., Napoly, A., Albergel, C., Mahfouf, J.-F., and Calvet, J.-C.: The effect of satellite-derived surface soil moisture and leaf area index land data assimilation on streamflow simulations over France, *Hydrology and Earth System Sciences*, 21, 2015–2033,
490 2017.
- Faroux, S., Kaptué Tchuenté, A. T., Roujean, J.-L., Masson, V., Martin, E., and Le Moigne, P.: ECOCLIMAP-II/Europe: a twofold database of ecosystems and surface parameters at 1 km resolution based on satellite information for use in land surface, meteorological and climate models, *Geoscientific Model Development*, 6, 563–582, <https://doi.org/10.5194/gmd-6-563-2013>, 2013.
- Friedl, M. and Sulla-Menashe, D.: MODIS/Terra+Aqua Land Cover Type Yearly L3 Global 0.05Deg CMG. NASA LP DAAC, Tech. rep.,
495 Boston University and MODAPS SIPS - NASA, <https://doi.org/10.5067/MODIS/MCD12C1.006>, 2015.
- Friedlingstein, P., O’Sullivan, M., Jones, M. W., Andrew, R. M., Hauck, J., Landschützer, P., Le Quéré, C., Li, H., Luijkx, I. T., Olsen, A., Peters, G. P., Peters, W., Pongratz, J., Schwingshackl, C., Sitch, S., Canadell, J. G., Ciais, P., Jackson, R. B., Alin, S. R., Arneeth, A., Arora, V., Bates, N. R., Becker, M., Bellouin, N., Berghoff, C. F., Bittig, H. C., Bopp, L., Cadule, P., Campbell, K., Chamberlain, M. A., Chandra, N., Chevallier, F., Chini, L. P., Colligan, T., Decayeux, J., Djeutchouang, L. M., Dou, X., Duran Rojas, C., Enyo, K., Evans,
500 W., Fay, A. R., Feely, R. A., Ford, D. J., Foster, A., Gasser, T., Gehlen, M., Gkritzalis, T., Grassi, G., Gregor, L., Gruber, N., Gürses, O., Harris, I., Hefner, M., Heinke, J., Hurtt, G. C., Iida, Y., Ilyina, T., Jacobson, A. R., Jain, A. K., Jarníková, T., Jersild, A., Jiang, F., Jin, Z., Kato, E., Keeling, R. F., Klein Goldewijk, K., Knauer, J., Korsbakken, J. I., Lan, X., Lauvset, S. K., Lefèvre, N., Liu, Z., Liu, J., Ma, L., Maksyutov, S., Marland, G., Mayot, N., McGuire, P. C., Metzl, N., Monacci, N. M., Morgan, E. J., Nakaoka, S.-I., Neill, C., Niwa, Y., Nützel, T., Olivier, L., Ono, T., Palmer, P. I., Pierrot, D., Qin, Z., Resplandy, L., Roobaert, A., Rosan, T. M., Rödenbeck, C., Schwinger,
505 J., Smallman, T. L., Smith, S. M., Sospedra-Alfonso, R., Steinhoff, T., Sun, Q., Sutton, A. J., Séférian, R., Takao, S., Tatebe, H., Tian, H., Tilbrook, B., Torres, O., Tourigny, E., Tsujino, H., Tubiello, F., van der Werf, G., Wanninkhof, R., Wang, X., Yang, D., Yang, X., Yu, Z., Yuan, W., Yue, X., Zaehle, S., Zeng, N., and Zeng, J.: Global Carbon Budget 2024, *Earth System Science Data*, 17, 965–1039, <https://doi.org/10.5194/essd-17-965-2025>, 2025.
- Garrigues, S., de Rosnay, P., Weston, P., Rüdiger, C., Bacour, C., Fairbairn, D., Vanderbecken, P., Rojas-Munoz, O., Pinnington, E., Agustí-Panareda, A., Boussetta, S., Calvet, J.-C., and Engelen, R.: Assimilation of solar-induced fluorescence satellite observations in the European Centre for Medium-Range Weather Forecasts integrated forecast system, *Quarterly Journal of the Royal Meteorological Society*, n/a, e70111, <https://doi.org/https://doi.org/10.1002/qj.70111>, e70111 QJ-25-0252, 2026.
- Gibelin, A.-L., Calvet, J.-C., Roujean, J.-L., Jarlan, L., and Los, S. O.: Ability of the land surface model ISBA-A-gs to simulate leaf area index at the global scale: Comparison with satellites products, *Journal of Geophysical Research: Atmospheres*, 111, 2006.



- 515 Guanter, L., Aben, I., Tol, P., Krijger, J. M., Hollstein, A., Köhler, P., Damm, A., Joiner, J., Frankenberg, C., and Landgraf, J.: Potential of the TROPospheric Monitoring Instrument (TROPOMI) onboard the Sentinel-5 Precursor for the monitoring of terrestrial chlorophyll fluorescence, *Atmospheric Measurement Techniques*, 8, 1337–1352, <https://doi.org/10.5194/amt-8-1337-2015>, 2015.
- Guanter, L., Bacour, C., Schneider, A., Aben, I., van Kempen, T. A., Maignan, F., Retscher, C., Köhler, P., Frankenberg, C., Joiner, J., and Zhang, Y.: The TROPOSIF global sun-induced fluorescence dataset from the Sentinel-5P TROPOMI mission, *Earth System Science Data*, 520 13, 5423–5440, <https://doi.org/10.5194/essd-13-5423-2021>, 2021.
- Hamer, P. D., Markelj, M., Rojas-Munoz, O., Bonan, B., Calvet, J.-C., Marécal, V., Guenther, A., Trimmel, H., Vallejo, I., Eckhardt, S., Sousa Santos, G., Sindelarova, K., Simpson, D., Schmidbauer, N., and Tarrasón, L.: Two Biogenic Volatile Organic Compound Emission Datasets over Europe Based on Land Surface Modelling and Satellite Data Assimilation, *Earth System Science Data Discussions*, 2025, 1–48, <https://doi.org/10.5194/essd-2025-442>, 2025.
- 525 Horowitz, C. A.: Paris Agreement, *International Legal Materials*, 55, 740–755, <https://doi.org/10.1017/S0020782900004253>, publisher: Cambridge University Press, 2016.
- Jacobs, C.: Direct impact of atmospheric CO₂ enrichment on regional transpiration, internal phd, wu, Netherlands, ISBN 9789054852506, <https://doi.org/10.18174/206972>, wU thesis 1772 Proefschrift Wageningen, 1994.
- Jacobs, C., Van den Hurk, B., and De Bruin, H.: Stomatal behaviour and photosynthetic rate of unstressed grapevines in semi-arid conditions, 530 *Agricultural and Forest Meteorology*, 80, 111–134, 1996.
- Jarlan, L., ALBERGEL, C., Bonan, B., Calvet, J.-C., DE ROSNAY, P., OTTLÉ, C., and PEYLIN, P.: Assimilation de données de télédétection pour le suivi des surfaces continentales, Inversion et assimilation de données de télédétection: Estimation des paramètres géophysiques, p. 45, 2023.
- Jiang, S., Zheng, Y., and Solomatine, D.: Improving AI system awareness of geoscience knowledge: Symbiotic integration of physical 535 approaches and deep learning, *Geophysical Research Letters*, 47, e2020GL088 229, 2020.
- Joiner, J., Yoshida, Y., Guanter, L., and Middleton, E. M.: New methods for the retrieval of chlorophyll red fluorescence from hyperspectral satellite instruments: simulations and application to GOME-2 and SCIAMACHY, *Atmospheric Measurement Techniques*, 9, 3939–3967, 2016.
- Jung, M., Schwalm, C., Migliavacca, M., Walther, S., Camps-Valls, G., Koirala, S., Anthoni, P., Besnard, S., Bodesheim, P., Carvalhais, N., 540 Chevallier, F., Gans, F., Goll, D. S., Haverd, V., Köhler, P., Ichii, K., Jain, A. K., Liu, J., Lombardozzi, D., Nabel, J. E. M. S., Nelson, J. A., O’Sullivan, M., Pallandt, M., Papale, D., Peters, W., Pongratz, J., Rödenbeck, C., Sitch, S., Tramontana, G., Walker, A., Weber, U., and Reichstein, M.: Scaling carbon fluxes from eddy covariance sites to globe: synthesis and evaluation of the FLUXCOM approach, *Biogeosciences*, 17, 1343–1365, <https://doi.org/10.5194/bg-17-1343-2020>, 2020.
- Köhler, P., Guanter, L., and Joiner, J.: A linear method for the retrieval of sun-induced chlorophyll fluorescence from GOME-2 and SCIA- 545 MACHY data, *Atmospheric Measurement Techniques*, 8, 2589–2608, <https://doi.org/10.5194/amt-8-2589-2015>, 2015.
- Köhler, P., Frankenberg, C., Magney, T. S., Guanter, L., Joiner, J., and Landgraf, J.: Global Retrievals of Solar-Induced Chlorophyll Fluorescence With TROPOMI: First Results and Intersensor Comparison to OCO-2, *Geophysical Research Letters*, 45, 10,456–10,463, <https://doi.org/https://doi.org/10.1029/2018GL079031>, 2018.
- Lang, S., Alexe, M., Chantry, M., Dramsch, J., Pinault, F., Raoult, B., Clare, M. C., Lessig, C., Maier-Gerber, M., Magnusson, L., et al.: 550 AIFS-ECMWF’s data-driven forecasting system, arXiv preprint arXiv:2406.01465, 2024.
- Leroux, D. J., Calvet, J.-C., Munier, S., and Albergel, C.: Using Satellite-Derived Vegetation Products to Evaluate LDAS-Monde over the Euro-Mediterranean Area, *Remote Sensing*, 10, <https://doi.org/10.3390/rs10081199>, 2018.



- LOBELIA: Revealing emission sources from space, <https://doi.org/10.5281/zenodo.10837172>, 2024.
- Lundberg, S. M. and Lee, S.-I.: A Unified Approach to Interpreting Model Predictions.
- 555 Lunel, T., Boone, A. A., and Le Moigne, P.: Irrigation strongly influences near-surface conditions and induces breeze circulation: Observational and model-based evidence, *Quarterly Journal of the Royal Meteorological Society*, 2024.
- Mahfouf, J.-F. and Bilodeau, B.: A simple strategy for linearizing complex moist convective schemes, *Quarterly Journal of the Royal Meteorological Society*, 135, 953–962, <https://doi.org/https://doi.org/10.1002/qj.427>, 2009.
- Mahfouf, J.-F., Bergaoui, K., Draper, C., Bouyssel, F., Taillefer, F., and Taseva, L.: A comparison of two off-line
560 soil analysis schemes for assimilation of screen level observations, *Journal of Geophysical Research: Atmospheres*, 114, <https://doi.org/https://doi.org/10.1029/2008JD011077>, 2009.
- Masson, V., Le Moigne, P., Martin, E., Faroux, S., Alias, A., Alkama, R., Belamari, S., Barbu, A., Boone, A., Bouyssel, F., et al.: The SURFEXv7. 2 land and ocean surface platform for coupled or offline simulation of earth surface variables and fluxes, *Geoscientific Model Development*, 6, 929–960, 2013.
- 565 Molnar, C.: *Interpretable machine learning*, Lulu. com, 2020.
- Moya, I., Camenen, L., Evain, S., Goulas, Y., Cerovic, Z., Latouche, G., Flexas, J., and Ounis, A.: A new instrument for passive remote sensing: 1. Measurements of sunlight-induced chlorophyll fluorescence, *Remote Sensing of Environment*, 91, 186–197, <https://doi.org/https://doi.org/10.1016/j.rse.2004.02.012>, 2004.
- Nelson, J. A., Walther, S., Gans, F., Kraft, B., Weber, U., Novick, K., Buchmann, N., Migliavacca, M., Wohlfahrt, G., Šigut, L., Ibrom, A.,
570 Papale, D., Göckede, M., Duveiller, G., Knohl, A., Hörtnagl, L., Scott, R. L., Dušek, J., Zhang, W., Hamdi, Z. M., Reichstein, M., Aranda-Barranco, S., Ardö, J., Op de Beeck, M., Billesbach, D., Bowling, D., Bracho, R., Brümmner, C., Camps-Valls, G., Chen, S., Cleverly, J. R., Desai, A., Dong, G., El-Madany, T. S., Euskirchen, E. S., Feigenwinter, I., Galvagno, M., Gerosa, G. A., Gielen, B., Goded, I., Goslee, S., Gough, C. M., Heinesch, B., Ichii, K., Jackowicz-Korczynski, M. A., Klosterhalfen, A., Knox, S., Kobayashi, H., Kohonen, K.-M., Korkiakoski, M., Mammarella, I., Gharun, M., Marzuoli, R., Matamala, R., Metzger, S., Montagnani, L., Nicolini, G., O’Halloran, T.,
575 Ourcival, J.-M., Peichl, M., Pendall, E., Ruiz Reverter, B., Roland, M., Sabbatini, S., Sachs, T., Schmidt, M., Schwalm, C. R., Shekhar, A., Silberstein, R., Silveira, M. L., Spano, D., Tagesson, T., Tramontana, G., Trotta, C., Turco, F., Vesala, T., Vincke, C., Vitale, D., Vivoni, E. R., Wang, Y., Woodgate, W., Yopez, E. A., Zhang, J., Zona, D., and Jung, M.: X-BASE: the first terrestrial carbon and water flux products from an extended data-driven scaling framework, *FLUXCOM-X, Biogeosciences*, 21, 5079–5115, <https://doi.org/10.5194/bg-21-5079-2024>, 2024.
- 580 Noilhan, J. and Mahfouf, J.-F.: The ISBA land surface parameterisation scheme, *Global and Planetary Change*, 13, 145–159, [https://doi.org/https://doi.org/10.1016/0921-8181\(95\)00043-7](https://doi.org/https://doi.org/10.1016/0921-8181(95)00043-7), soil Moisture Simulation, 1996.
- Noilhan, J. and Planton, S.: A Simple Parameterization of Land Surface Processes for Meteorological Models, *Monthly Weather Review*, 117, 536 – 549, [https://doi.org/10.1175/1520-0493\(1989\)117<0536:ASPOLS>2.0.CO;2](https://doi.org/10.1175/1520-0493(1989)117<0536:ASPOLS>2.0.CO;2), 1989.
- Rascher, U., Alonso, L., Burkart, A., Cilia, C., Cogliati, S., Colombo, R., Damm, A., Drusch, M., Guanter, L., Hanus, J., et al.: Sun-induced
585 fluorescence—a new probe of photosynthesis: First maps from the imaging spectrometer HyPlant, *Global change biology*, 21, 4673–4684, 2015.
- Ricart, S., Ribas, A., and Pavón, D.: Qualifying irrigation system sustainability by means of stakeholder perceptions and concerns: lessons from the Segarra-Garrigues Canal, Spain, *Natural Resources Forum*, 40, 77–90, <https://doi.org/https://doi.org/10.1111/1477-8947.12097>, 2016.
- 590 Richards, L. A.: Capillary conduction of liquids through porous mediums, *physics*, 1, 318–333, 1931.



- Rossini, M., Nedbal, L., Guanter, L., Ač, A., Alonso, L., Burkart, A., Cogliati, S., Colombo, R., Damm, A., Drusch, M., et al.: Red and far red Sun-induced chlorophyll fluorescence as a measure of plant photosynthesis, *Geophysical research letters*, 42, 1632–1639, 2015.
- Rüdiger, C., Albergel, C., Mahfouf, J.-F., Calvet, J.-C., and Walker, J. P.: Evaluation of the observation operator Jacobian for leaf area index data assimilation with an extended Kalman filter, *Journal of Geophysical Research: Atmospheres*, 115, 595 <https://doi.org/https://doi.org/10.1029/2009JD012912>, 2010.
- Sabater, J. M., Rüdiger, C., Calvet, J.-C., Fritz, N., Jarlan, L., and Kerr, Y.: Joint assimilation of surface soil moisture and LAI observations into a land surface model, *Agricultural and Forest Meteorology*, 148, 1362–1373, <https://doi.org/https://doi.org/10.1016/j.agrformet.2008.04.003>, 2008.
- Schmidhuber, J.: Deep learning in neural networks: An overview, *Neural networks*, 61, 85–117, 2015.
- 600 Sun, Y., Fu, R., Dickinson, R., Joiner, J., Frankenberg, C., Gu, L., Xia, Y., and Fernando, N.: Drought onset mechanisms revealed by satellite solar-induced chlorophyll fluorescence: Insights from two contrasting extreme events, *Journal of Geophysical Research: Biogeosciences*, 120, 2427–2440, 2015.
- Sun, Z., Sandoval, L., Crystal-Ornelas, R., Mousavi, S. M., Wang, J., Lin, C., Cristea, N., Tong, D., Carande, W. H., Ma, X., et al.: A review of earth artificial intelligence, *Computers & Geosciences*, 159, 105 034, 2022.
- 605 Trimmel, H., Hamer, P., Mayer, M., Schreier, S. F., Weihs, P., Eitzinger, J., Sandén, H., Fitzky, A. C., Richter, A., Calvet, J.-C., Bonan, B., Meurey, C., Vallejo, I., Eckhardt, S., Santos, G. S., Oumami, S., Arteta, J., Marécal, V., Tarrasón, L., Karl, T., and Rieder, H. E.: The influence of vegetation drought stress on formaldehyde and ozone distributions over a central European city, *Atmospheric Environment*, 304, 119 768, <https://doi.org/https://doi.org/10.1016/j.atmosenv.2023.119768>, 2023.
- Veefkind, J., Aben, I., McMullan, K., Förster, H., de Vries, J., Otter, G., Claas, J., Eskes, H., de Haan, J., Kleipool, Q., van 610 Weele, M., Hasekamp, O., Hoogeveen, R., Landgraf, J., Snel, R., Tol, P., Ingmann, P., Voors, R., Kruizinga, B., Vink, R., Visser, H., and Levelt, P.: TROPOMI on the ESA Sentinel-5 Precursor: A GMES mission for global observations of the atmospheric composition for climate, air quality and ozone layer applications, *Remote Sensing of Environment*, 120, 70–83, <https://doi.org/https://doi.org/10.1016/j.rse.2011.09.027>, the Sentinel Missions - New Opportunities for Science, 2012.